# An Asynchronously Excited Brushless Wound Field Synchronous Machine

Dorsa Talebi[1], *Student Member, IEEE,* Matthew C Gardner[2], *Member, IEEE*, S. Mehdi Seyedi[1], *Student Member, IEEE,* and Hamid A. Toliyat[1], *Fellow, IEEE*

***Abstract* --This paper proposes a novel brushless wound field synchronous machine with only one set of stator windings. Employing the principles of pole phase modulation, two independent spatial harmonics are created: one rotates synchronously and the other rotates asynchronously to induce current on an extra set of rotor windings called the induction winding. This current is rectified and supplied to the rotor field winding. The stator current excitations are defined to provide independent control over the speed and magnitude of the two spatial flux harmonics. Furthermore, this approach allows for self-starting from zero speed. The impacts of varying the speed and magnitude of the harmonics on the motor performance for traction application is studied with FEA. This topology eliminates the need of brushes in wound field synchronous machines; however, the induction torque can be offset by the increased saturation in the machine due to the presence of the asynchronous harmonic.**

***Index Terms*— Brushless, field weakening, spatial harmonics, induction excitation, pole phase modulation, self-excitation, self-starting, wound field synchronous machine (WFSM), traction application**

## I. Introduction

Permanent magnet (PM) machines are employed by most major electric vehicle (EV) manufacturers, due to their high torque density and efficiency. However, PM machines tend to have several disadvantages, such as high core losses at high speed, volatile PM prices, susceptibility to faults, and limited field weakening capability, which leads to a search for other alternatives [1]-[5]. Conventional wound field synchronous machines (WFSMs) could potentially be a substitute for PM machines. However, the additional brushes and slip ring or the pilot excitation system consume additional space and create losses, and the brushes may increase maintenance requirements or produce sparking [4].

Over the years, researchers have proposed various alternative brushless excitation strategies for inducing a current on the rotor to excite the field winding as a wireless excitation of the rotor current [1], [4] and [5]. However, many of these brushless excitation strategies, such as rotating transformers, electromagnetic coupling resonators, or capacitive non-contact power transfer, employ additional wireless excitation systems beyond the main portion of the motor, which increase the motor's overall size, mass, and cost [1], [4]-[5].

Other studies utilize existing time or space harmonics in the main body of the motor to induce current in an extra set of rotor windings. This current is rectified and supplied to the field winding of the WFSM. However, the pulsating magnetomotive force (MMF) used to induce current on the rotor is often not fully independent from the main MMF component used to generate torque, which may result in considerable torque ripple. Additionally, in this case, the design cannot start from zero speed in motoring operation, even with an inverter, and the field current cannot be controlled independently of the armature current. For example, [6] uses a fractional-slot concentrated winding with 18 teeth and 10 poles and produces spatial harmonics with 5 and 13 pole pairs simultaneously using the same principles as a Vernier machine. This technique has the advantage of not requiring extra switches or coils on the stator but lacks independent control of the field and armature currents and cannot be used to start a motor from rest.

However, some of the approaches with an independent control over field and armature current, have the disadvantage of requiring a dual inverter configuration, which increases the cost, size, and complexity of the system [7], [8]. In [9] the starting problem is addressed through a proposed double three-phase winding and dual inverter with a neutral connection. Nonetheless, this approach increases cost and complexity.

Additionally, [10]-[12] feed the brushless synchronous machine's field winding using the induction excitation concept. The induction flux is produced using an extra three-phase winding on the stator. In these models, the extra stator winding has a different number of pole pairs than the main stator winding; thus, the resultant spatial MMFs harmonics in the airgap are independent from each other to prevent excessive torque ripple. Although this provides the ability to start at zero speed, the need for extra stator coils and an extra inverter to control it is a significant disadvantage. On the other hand, [13] proposes a configuration of independent harmonic currents on the same physical set of winding on stator utilizing power electronic devices. The paper provides an analytical equation, and evaluates a few different winding arrangements, and pole count combinations. Furthermore, the different discussed topologies are briefly compared based on the harmonic winding factor, leakage of harmonic winding, copper losses due to the harmonic winding, and the machine rating. However, this has disadvantages of using some of the DC link voltage for harmonic injection and high saturation.

D. Talebi is with Department of Electrical and Computer Engineering, Texas A&M University, College Station, TX 77843, USA (e-mail: dorsa.talebi@tamu.edu)

M. C. Gardner is with Department of Electrical and Computer Engineering, University of Texas at Dallas, Richardson, TX 75080, USA (e-mail: Matthew.Gardner@utdallas.edu)

S. M. Seyedi is with Department of Electrical and Computer Engineering, Texas A&M University, College Station, TX 77843, USA (e-mail: mehdiseyedi@tamu.edu)

H. A. Toliyat is with Department of Electrical and Computer Engineering, Texas A&M University, College Station, TX 77843, USA (e-mail: toliyat@tamu.edu)

This paper proposes the asynchronously excited synchronous machine (AESM), as a variation of the induction excitation concept using the existing stator windings to create flux with two main spatial harmonics, one of which rotates synchronously while the other rotates asynchronously [14]. The synchronous harmonic interacts with flux created by the field winding to produce torque, while the asynchronous harmonic is used to induce current on the rotor. Both of these spatial flux harmonics are created using a single set of stator windings via pole phase modulation [15]-[17], and, since the concept of induction excitation is being used, the machine is able to start from zero speed. This bears some similarities to the concept presented in [13], but the combination of slots, poles, and phases in this paper yields higher winding factors than those in [13]. Unlike [13], this paper evaluates a range of different operating conditions to characterize the machine's performance more broadly with an analysis of the torque contribution of the synchronous and asynchronous harmonics and studies the saturation effect on the AESM concept.

## II. Concept and Operating Principle

To implement independent control of the two different spatial flux harmonics, this design employs the same principles as pole phase modulation, which is used in induction machines to change the pole count between low-speed and high-speed operating modes [15]-[17]. This provides independent control of the field and armature currents. Depending on the design specification, different combinations of pole counts can be created for the two spatial harmonics using different numbers of slots and phases, such as six-pole and four-pole in 36 slots or six-pole and two-pole in 18 slots. In this paper, a nine-phase winding is used to simultaneously produce six-pole and two-pole magnetic flux harmonics with independent rotational speeds and flux magnitudes.

Fig. 1 shows the stator winding arrangement of nine-phase configuration capable of producing independent two-pole and six-pole magnetic fields. Common-mode current in the three phases of a single color (eg. 1, 4, and 7) produces a six-pole magnetic field. The two-pole magnetic field is produced with different currents in each of the nine phases. The current of the n$^{th}$ phase, $i_n$ is

$$i_n = \sqrt{2}I_A \cos\left(\omega_A t + \theta_A - \frac{2(n-1)\pi}{9}\right) + \sqrt{2}I_S \cos\left(\omega_S t + \theta_S - \frac{6(n-1)\pi}{9}\right), \quad (1)$$

where $I_A$ and $I_S$ are the RMS values of the two-pole and six-pole currents, respectively, $\omega_A$ and $\omega_S$ are their respective frequencies, and $\theta_A$ and $\theta_S$ are their respective angular offsets in electrical degrees. These nine currents can be supplied by a single nine-phase inverter.

By applying winding function theory, independent control of the two spatial harmonics on the resultant stator MMF, can be demonstrated. The winding function of the n$^{th}$ phase, $N_n$, can be generally expressed in terms of Fourier series components,

$$N_n(\varphi) = \sum_{h=1,3,5,\dots}^{\infty} N_h \cos\left(h\varphi - h(n-1)\frac{2\pi}{9}\right), \quad (2)$$

where $N_h$ represents the magnitude of the $h^{th}$ harmonic component and $\varphi$ represents the mechanical angle.

Then, the MMF for each phase can be expressed as the product of its winding function and current. The total MMF from all nine phases, $\mathcal{F}_{Total}$, is

$$\begin{aligned}\mathcal{F}_{Total} = {} & \frac{9\sqrt{2}}{2} I_A \sum_{h=17,35,53,\dots}^{\infty} N_h \cos(h\varphi + \omega_A t + \theta_A) \\ & + \frac{9\sqrt{2}}{2} I_A \sum_{h=1,19,37,55,\dots}^{\infty} N_h \cos(h\varphi - \omega_A t - \theta_A) \\ & + \frac{9\sqrt{2}}{2} I_S \sum_{h=15,33,51,\dots}^{\infty} N_h \cos(h\varphi + \omega_S t + \theta_S) \\ & + \frac{9\sqrt{2}}{2} I_S \sum_{h=3,21,39,57,\dots}^{\infty} N_h \cos(h\varphi - \omega_S t - \theta_S) \quad (3)\end{aligned}$$

Thus, the total MMF has four separate sets of spatial harmonics. For both $I_A$ and $I_S$, there is a set of forward rotating harmonics and a set of reverse rotating harmonics, and none of the spatial harmonics appear in multiple sets of harmonics. This indicates that there is no interaction between the fields produced by the synchronous and asynchronous currents (neglecting the effects of saturation). In this case, the $h$ = 1 (two-pole) and $h$ = 3 (six-pole) spatial harmonics are used as the asynchronous and synchronous harmonics, respectively. As demonstrated by (3), the magnitudes, speeds, and phase angles of these two harmonics can be controlled independently, which can reduce torque ripple, vibrations, and acoustic noise. However, in practice, saturation may prevent the spatial harmonics from being completely independent.

The rotor is equipped with two sets of windings and a rectifier, as shown in Fig. 2. Each set of windings on the rotor has the same number of poles as one of the spatial flux harmonics produced by the stator. The two-pole MMF produced by the stator rotates asynchronously to induce a current in the two-pole, three-phase rotor induction winding. The six-pole field winding is connected via a three-phase rectifier to the two-pole rotor induction winding. The DC rectified current serves as the synchronous motor field current

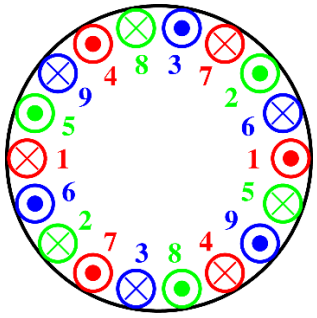


Fig. 1. Stator winding arrangements for a nine-phase motor capable of producing independent two-pole and six-pole fields

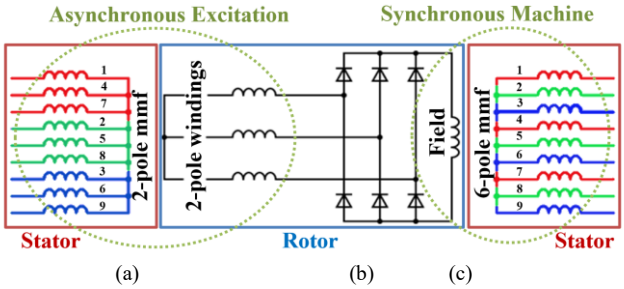


Fig. 2. Example winding arrangement with (a) a nine-phase, two-pole winding arrangement on the stator inducing a current in a three-phase, two-pole winding on the rotor, which is (b) rectified. (c) The rectified current excites the six-pole field winding on the rotor, which interacts with the three-phase, six pole winding on the stator.

and interacts with the synchronous six-pole flux harmonic produced by the stator to produce torque.

## III. Finite Element Analysis of Proposed Topology

A 2-D finite element analysis (FEA) model, Fig. 3, was created in ANSYS Maxwell to evaluate an example motor and analyze its performance. As in the previous section, the two-pole harmonic is used as the asynchronous harmonic, while the six-pole harmonic serves as the synchronous harmonic. Table I summarizes the geometric parameters of the FEA model. A 25 $A_{rms}/mm^2$ current density is selected to be comparable to liquid-cooled traction motors [18]. Table II gives the parameters related to the synchronous and asynchronous harmonics.

The operating principle of the machine is a synchronous motor with asynchronous excitation of the field current. In Table II, asynchronous current distribution (ACD) defines what percentage of the total RMS current in the stator windings is to being utilized for the asynchronous two-pole component with $\omega_A$ frequency, while the rest of the stator current is used generate the six-pole synchronous harmonic, which is responsible for producing the main electromagnetic torque by interacting with the rotor field magnetic flux. This relationship is expressed by

$$I_A = (ACD)I_{total} \quad (4)$$

$$I_{total} = \sqrt{I_A^2 + I_S^2}, \quad (5)$$

where $I_{total}$ is the total RMS current in each stator phase. (Note that the current distributions in Table II add up to more than 100% because they are based on the total RMS as in (4)).

Fig. 4(a) shows the radial flux density produced in the airgap resulting from the stator excitation stated in (1) for a current density of 10 A/mm$^2$ and ACD of 15% for M19 cores and for cores made of a hypothetical magnetically linear steel (to exclude the effect of saturation). Fig. 4(b) provides the fast Fourier transform (FFT) of the radial flux density in the airgap peripheral for the nonlinear steel, while Fig. 4(c) shows the FFT of the radial flux density for the linear steel. The major components that appear in the spectrum are the harmonic orders derived in (3). However, a comparison of Fig. 4(b) and (c) illustrates that saturation produces small-magnitude harmonics that do not appear in (3), such as the fifth harmonic. The UVW set of windings refers to the two-pole induction rotor winding while the F winding is the field winding. The

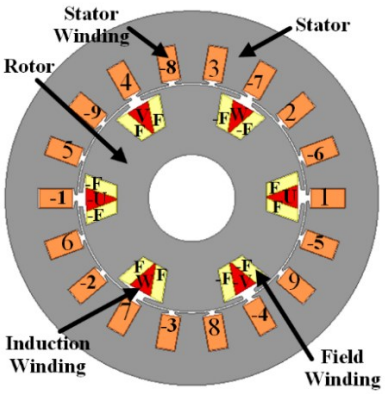


Fig 3. The finite element model

TABLE I
Design Parameters

| Parameter | Unit | Value |
|---|---|---|
| Stator Outer Diameter | mm | 215 |
| Stator Inner Diameter | mm | 132 |
| Stack Length | mm | 125 |
| Air gap Length | mm | 0.7 |
| Stator Number of Slots | | 18 |
| Rotor Number of Slots | | 6 |
| Stator Winding Turns | | 35 |
| Number of Phases | | 9 |
| Reference Speed | rpm | 1800 |
| Copper Fill Factor | | 0.6 |
| RMS Stator Current Density | A/mm$^2$ | 25 |

TABLE II
Synchronous and Asynchronous Parameters

| Parameter | Synchronous | Asynchronous |
|---|---|---|
| Number of Poles | 6 | 2 |
| Stator Excitation Frequency | 90 Hz | 150 Hz |
| Current Distribution | 96.8% | 25.0% |
| Rotor Field Winding Turns | 160 | - |
| Rotor Induction Winding Turns | - | 60 |

excitation of each winding on the stator, represents both two-pole and six-pole current excitation components with their separate amplitude and frequencies, as exemplified in (1).

Based on the operating principles of an induction machine, the two-pole 150 Hz asynchronous excitation from the stator induces a three- phase voltage in the rotor induction windings with a slip frequency of 120 Hz, when the rotor speed is 1800 rpm. Fig. 5 shows FEA flux density plot, in which the six- pole

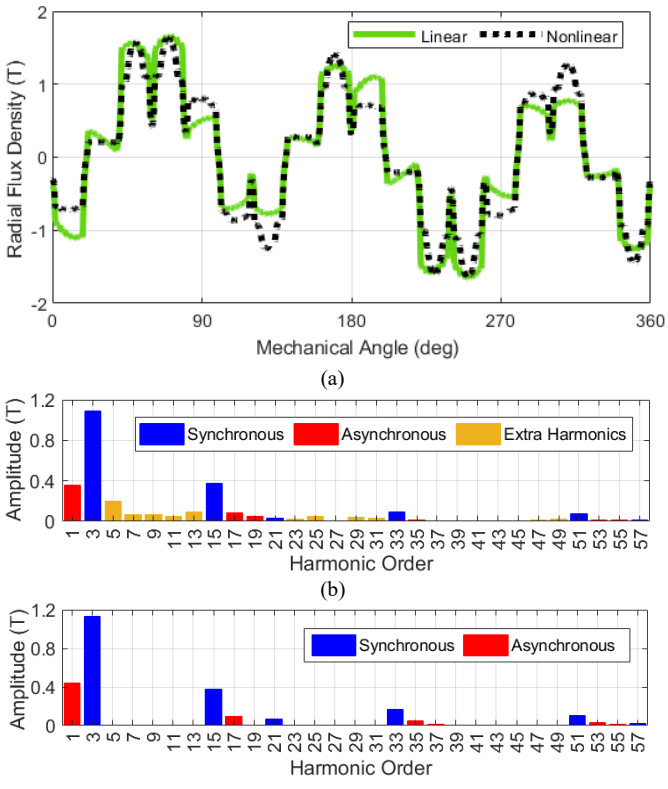


Fig. 4. FEA results of 10 A/mm$^2$ and 15% ACD (a) Airgap radial flux density of nonlinear and linear steel, (b) FFT of the flux density with nonlinear steel, (c) FFT of the flux density with linear steel

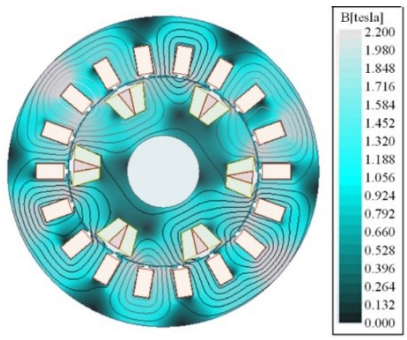


Fig 5. Flux density plot on core material

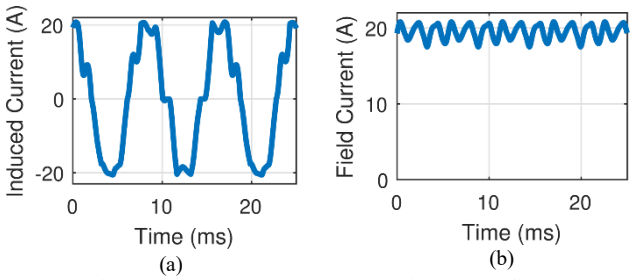


Fig. 6. (a) Induced current in one of the rotor induction windings (Phase U) and in the (b) field winding (F coils) current

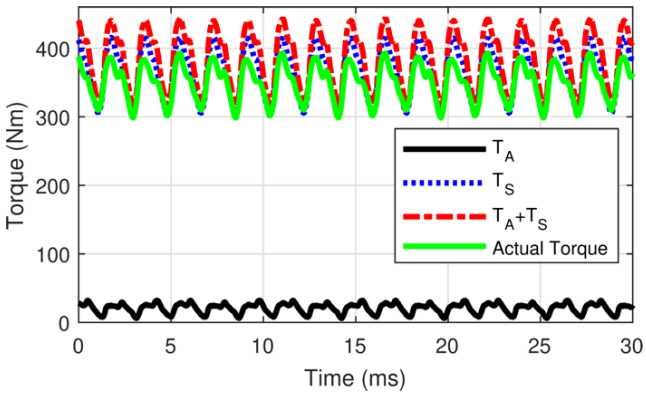


Fig. 7. Actual torque of the example machine, torque produced by the asynchronous portion of the machine ($T_A$), torque produced by synchronous portion of the machine ($T_S$), and the sum of the synchronous and asynchronous torques ($T_A$+$T_S$)

dominant flux is affected by the two-pole flux.

Fig. 6(a) shows the induced current on one of the rotor induction windings with 120 Hz frequency, and Fig. 6(b) shows the field current, which is rectified from the rotor induction currents. The actual electromagnetic torque is shown in Fig. 7. This torque includes the torques of two machines, asynchronous machine, and an asynchronous machine. In order to separate these torques, a new set of simulations were defined. To model the synchronous-only machine, the currents in the induction rotor windings (UVW) were set to zero, and the field winding fed by a DC current source based on the average field current observed in the whole machine. Additionally, the stator was excited with only the synchronous component of the stator current. Similarly, the asynchronous-only machine was set up with zero current in the field winding, and the output of the rectifier was instead connected to an equivalent resistance and inductance. In this case, the stator was excited with only the asynchronous component of the stator current. Fig. 7 also shows the torques produced by the asynchronous and synchronous portions of the machine and compares the sum of the torques produced by the separate operations with the torque produced by the whole machine. The average of actual torque of the whole machine is 350 Nm while the average of the sum of the asynchronous and synchronous torques from the separate simulations is 385 Nm. The dominant source of torque ripple is the slotting harmonics, which can be mitigated by skewing or tooth shaping. Also, this can be reduced with other combinations of pole pairs and slots.

## IV. IV. LINEAR SIMULATIONS AND THE IMPACT OF SATURATION

Fig. 7 shows that the average torque produced by the whole machine is about 9% lower than the average sum of the synchronous and asynchronous torques. As the equations derived in Section II indicate independent spatial flux harmonics, the previous simulations were repeated using a hypothetical linear BH curve for the stator and rotor cores with $\mu_r$ selected to yield a similar torque as the nonlinear model, instead of the nonlinear steel BH curves used in previous simulations, to model the motor without saturation. Table III summarizes the results of both the linear and nonlinear simulations. For the case without saturation, the sum of the asynchronous and synchronous torques almost exactly matches the torque of the complete machine. (Note that the rotor leakage inductances of the linear case are much larger than those in the saturated case, which can explain why the linear case produces less asynchronous torque.) Thus, saturation is the cause of the discrepancy in Fig. 7. This reveals an inherent disadvantage of the induction excitation scheme for brushless WFSMs: the flux required to excite the rotor current reduces the amount of flux that can be used for primary synchronous operation. Thus, although the induction excitation scheme eliminates the need for adding an extra section to the motor for the purposes of rotor current excitation, it can reduce the torque density of the motor itself, especially when operating in highly saturated conditions. In the case of the proposed machine, this is partially mitigated by using the asynchronous excitation of the rotor currents to generate some small positive torque, but the small induction torque will not outweigh the impacts of increased saturation when the machine is operating with high flux densities.

## V. Impact of Changing Field Current Control Parameters

The stator current is separated into two parts, one of which is used to generate the synchronous harmonic while the other generates the asynchronous harmonic, which is used to excite the rotor field current. There are two parameters that can be used to control the field current. The first parameter is the amount of stator current used to generate the asynchronous harmonic. For a fixed stator current density, this is reflected in the ACD. The second parameter that can be used to control the field current is the slip frequency of the asynchronous harmonic. Fig. 8 shows the impacts of varying these two parameters for simulations with ACD of 15%, 25%, and 35% at asynchronous current frequencies from 50 Hz to 250 Hz

TABLE III
COMPARISON OF LINEAR/NO SATURATION AND NONLINEAR/SATURATED SIMULATIONS

| Operation | RMS Stator Current (A) | | Avg Torque (Linear) (Nm) | Avg Torque (Nonlinear) (Nm) |
|---|---|---|---|---|
| | $I_A$ | $I_S$ | | |
| Synchronous | - | 85.5 | 364 | 364 |
| Asynchronous | 22.1 | - | 10 | 21 |
| Complete | 22.1 | 85.5 | 377 | 350 |

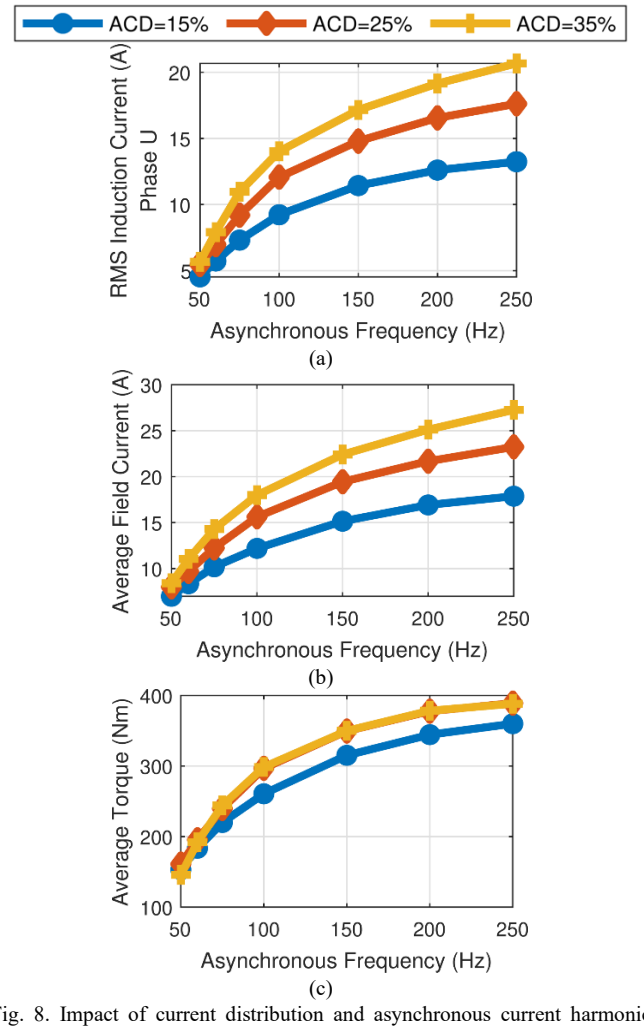


Fig. 8. Impact of current distribution and asynchronous current harmonic frequency on (a) the RMS induced current in a rotor induction winding, (b) the average induced rotor field current, and (c) the average torque of the whole machine.

(slip frequencies from 20 Hz to 220 Hz for a synchronous speed of 1800 rpm). Increasing the magnitude of either the asynchronous current or the slip frequency will increase the induced current in the rotor induction windings, as shown in Fig. 8(a), which increases the average field current, as shown in Fig. 8(b). Since the torque of a synchronous machine is proportional to the current flowing in the stator winding times the rotor flux, which is proportional to the field current if saturation is neglected, the increase in field current in Fig. 8(b) is generally reflected by an increase in average torque in Fig. 8(c). However, increasing the asynchronous component of the stator current reduces the synchronous component of the stator current for a fixed stator current density. Together with the impact of saturation, this means that the highest asynchronous current component does not always produce the highest overall torque. On the other hand, increasing the asynchronous frequency may increase the voltages that the inverter is required to supply.

Figs. 9(a) and (b) represent the impacts of the asynchronous frequency and ACD on the synchronous and induction torques. The synchronous torque follows a similar pattern to the overall average torque in Fig. 8(c). However, the induction torque behaves differently; increasing the ACD consistently increases the induction torque. Additionally, the induction torque is maximized at some nontrivial slip frequency. However, because the induction torque is such a small portion of the overall torque for this particular design, these trends are not evident in Fig. 8(c).

Figs. 10(a) and (b) shows how changing ACD and asynchronous frequency affect the copper losses and core losses, respectively. Ultimately, the efficiency results in Fig. 10(c) show that the large copper losses with higher ACD result in poor efficiency. The low range of efficiencies can potentially be improved by design optimization or by operating at a lower current density. A comparison of Figs. 8(c), 10(a) and 10(c) indicates that operating at a higher slip frequency with a lower ACD may be the optimal way to achieve a target torque with minimal copper losses and enhanced efficiency. Fig 10(d) provides the starting torque with zero synchronous speed and slip frequencies similar to the 1800 rpm studies. The results show that the motor can start from rest with the asynchronous excitation method.

So far in this paper, all the previous simulations were based on 25 $A_{rms}/mm^2$ current density. However, for traction applications, it is necessary to study the EM performance of the motor at different operating points; therefore, a study of changing the current density with 1, 5, 10, 15, 20 $A_{rms}/mm^2$ values have been performed with varying asynchronous frequencies and ACDs. The impact on EM torque from changing ACD from 25% to 35% is extremely minor at most of the current densities. This is likely due to saturation, as at a current density of 1 $A/mm^2$, there was an approximately 30% difference in average torque between the 25% and 35% ACD cases. Moreover, the flux plots for 5 $A/mm^2$ with 15% and 35% ACDs shown in Figs. 11(a) and (b) illustrates that for the same

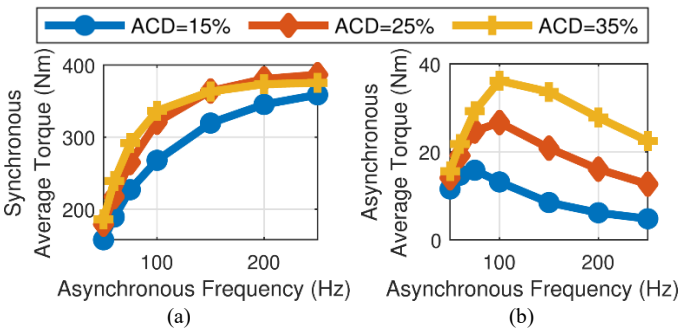


Fig. 9. Impact of asynchronous current distribution and asynchronous current harmonic frequency on (a) torque produced by the synchronous portion of the machine and (b) torque produced by the asynchronous portion of the machine

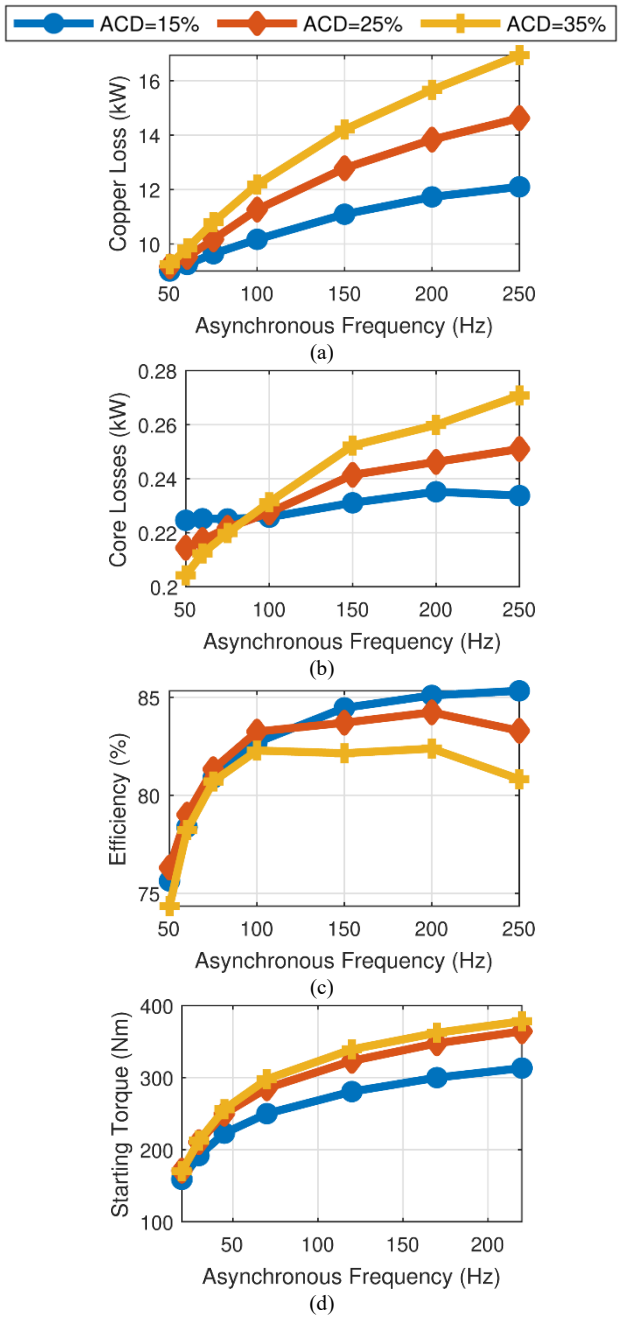


Fig. 10. Impact of asynchronous current distribution and asynchronous current harmonic frequency on (a) copper losses, (b) core losses, (c) efficiency at 1800 rpm and (d) average starting torque at zero speed

total stator current, when a larger amount of current is injected into 2 pole operation, the model experiences more saturation. On the other hand, Figs. 12(a) and (b) illustrate the average torque and efficiency at different asynchronous frequencies and current densities with 25% ACD. As the copper losses are the dominant source of losses in this range of current densities, reducing the current density tends to increase efficiency. The AESM concept provides flexible control for the motor employing the three control parameters, ACD, current/current density, and asynchronous frequency. However, for one single ACD, the results of Fig. 12 (a) and (b) indicate that to obtain amid-range torque, a higher frequency with lower current density can increase efficiency by reducing copper losses.

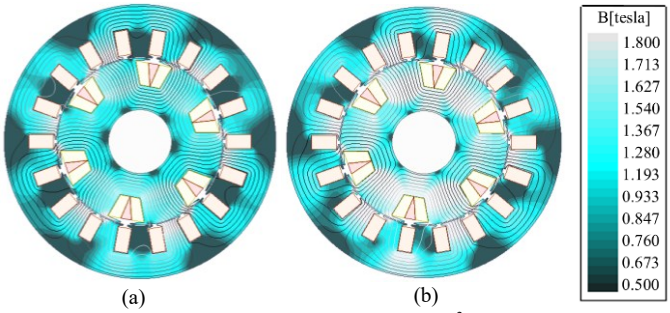


Fig. 11. Flux density plot on core material at 5 A/mm$^2$ current density (a) 15% ACD (b) 35% ACD

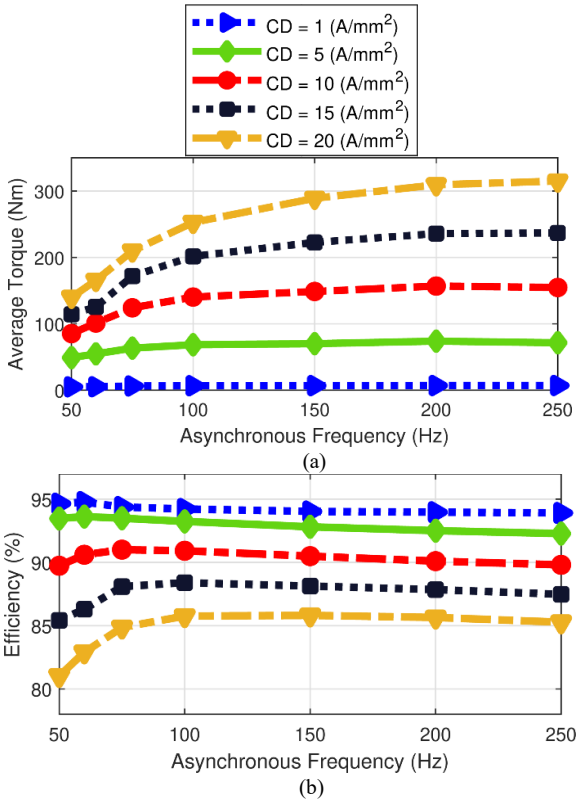


Fig. 12. Impact of varying current density and asynchronous frequency for 25% ACD on (a) torque and (b) efficiency.

## VI. Negative Slip Frequency Excitation

The machine can also be operated with negative slip frequency using an asynchronous current frequency lower than the synchronous frequency of the rotor, which is 30 Hz for

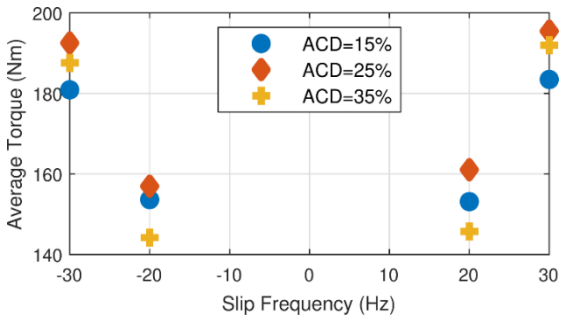


Fig. 13. Impact of asynchronous current distribution and slip frequency on the average torque of the whole machine for positive and negative slip frequencies with the same magnitudes

this1800 rpm example. This will still induce a current in the rotor induction winding to excite the rotor field winding. In the positive slip frequency cases, both the asynchronous and synchronous torques are positive, but a negative slip frequency will result in negative induction torque, reducing the overall torque. Fig. 13 compares the average torque with positive and negative slip frequencies with the same magnitudes in each case. While this negative slip frequency does reduce the torque slightly, it can also reduce the voltage requirements of the inverter, especially at high rotor speeds.

## VII. Conclusion

The proposed AESM, effectively combines an induction motor and a synchronous motor that share the same stator windings, stator steel, and rotor steel, as well as the same housing, bearings, and cooling. The rotor windings of the induction motor are connected to a rectifier, which supplies DC current to the field winding of the synchronous motor's rotor. A single set of stator windings can create two independent spatial harmonics through the principles of pole phase modulation which requires a multiphase inverter; these two spatial harmonics are used to drive the two motors. Thus, the proposed means of exciting the field current has advantages over other excitation strategies. First, no brushes or slip rings are required to transfer current to the rotor. Second, although the rotor excitation consumes an existing portion of the electromagnetic capability of the motor, it only employs an additional winding and rectifier on the rotor without the need of introducing an extra volume for a separate exciter system for the motor. Third, an induction motor serves as the means of exciting the rotor field current, which means that the process of exciting the rotor field current also produces some useful torque. Finally, the proposed scheme offers extremely flexible control employing the three control parameters, ACD, current/current density, and asynchronous frequency to allow for optimization of the efficiency across a wide range of operating points. Future work includes an optimization study and a prototype of the topology.

## VIII. Acknowledgment

Portions of this research were conducted with the advanced computing resources provided by Texas A&M High Performance Research Computing. The authors would like to thank ANSYS for their support of the EMPE lab through the provision of FEA software.

## IX. References

[1] C. Stancu, T. Ward, K. Rahman, R. Dawsey, and P. Savagian, "Separately excited synchronous motor with rotary transformer for hybrid vehicle application," in *Proc. IEEE Energy Convers. Congr. and Expo.*, 2014, pp. 5844-5851.

[2] D. G. Dorrell, "Are wound-rotor synchronous motors suitable for use in high efficiency torque-dense automotive drives?," in *Proc. Annual Conf. on IEEE Ind. Electron. Soc.*, 2012, pp. 4880-4885.

[3] T. A. Lipo and Z. S. Du, "Synchronous motor drives-a forgotten option," in *Proc. Int. Aegean Conf. on Elect. Mach. & Power Electron*., 2015.

[4] A. Di Gioia et al., "Design and Demonstration of a Wound Field Synchronous Machine for Electric Vehicle Traction With Brushless Capacitive Field Excitation," *IEEE Trans. Ind. Appl.*, vol. 54, no. 2, pp. 1390-1403, Mar.-Apr. 2018.

[5] T. Raminosoa and R. Wiles, "Contactless Rotor Excitation for Traction Motors," in *Proc. IEEE Energy Convers. Congr. and Expo.*, 2018, pp. 6448-6453.

[6] G. Dajaku and D. Gerling, "New self-excited synchronous machine with tooth concentrated winding," in *Proc. Int. Elec. Drives Production Conf.* 2013, pp. 1-6.

[7] F. Yao, Q. An, X. Gao, L. Sun, and T. A. Lipo, "Principle of Operation and Performance of a Synchronous Machine Employing a New Harmonic Excitation Scheme," *IEEE Trans. Ind. Appl.*, vol. 51, no. 5, pp. 3890-3898, Sep.-Oct. 2015.

[8] Q. Ali, T. A. Lipo, and B. Kwon, "Design and analysis of a novel brushless wound rotor synchronous machine," in *Proc. IEEE Int. Magn. Conf.*, 2015, pp. 1-1.

[9] F. Yao, D. Sun, L. Sun, and T. A. Lipo, "Dual Third-Harmonic-Current Excitation Principle of a Brushless Synchronous Machine Based on Double Three-Phase Armature Windings," in *Proc. Int. Conf. Elec. Mach. and Sys*, 2019, pp. 1-4.

[10] C. Chakraborty, Y. T. Rao, and H. Bhattacherjee, "Brushless induction excited synchronous motor (BinSyM): A new motor for high power applications," in *Proc. IEEE Power India Int. Conf.*, 2016, pp. 1-6.

[11] C. Chakraborty and Y. T. Rao, "Performance of Brushless Induction Excited Synchronous Generator," *IEEE J. of Emerg. and Sel. Topics in Power Electron.*, vol. 7, no. 4, pp. 2571-2582, Dec. 2019.

[12] Y. T. Rao, C. Chakraborty, and S. Basak, "Brushless Induction Excited Synchronous Generator With Induction Machine Operating in Plugging Mode," *IEEE Trans. Ind. Appl.*, vol. 54, no. 6, pp. 5748-5759, Nov.-Dec. 2018.

[13] J. Potter, M. Pfost, and G. Schullerus "Topology Analysis of Harmonic-Excited Wound-Rotor Synchronous Machines," *in Proc. IEEE Int. Elect. Mach. Drives Conf.,* 2021*,* pp. 1-7.

[14] H. A. Toliyat, M. C. Gardner, and D. Talebi. "Method and system for brushless wound field synchronous machines." U.S. Patent Application 17/236,764, filed October 28, 2021.

[15] J. W. Kelly, E. G. Strangas, and J. M. Miller, "Multiphase space vector pulse width modulation," *IEEE Trans. Energy Convers.*, vol. 18, no. 2, pp. 259-264, June 2003.

[16] M. P. Magill, P. T. Krein, and K. S. Haran, "Equivalent circuit model for pole-phase modulation induction machines," in *Proc. IEEE Int. Elect. Mach. Drives Conf.*, 2015, pp. 293-299.

[17] B. Ge, D. Sun, W. Wu, and F. Z. Peng, "Winding Design, Modeling, and Control for Pole-Phase Modulation Induction Motors," *IEEE Trans. Magn.*, vol. 49, no. 2, pp. 898-911, Feb. 2013.

[18] J. R. Hendershot and T. J. E. Miller, *Design of Brushless Permanent-Magnet Machines*, Oxford: Clarendon Press, 1994.

## X. Biographies

**Dorsa Talebi** (S'18) received the B.S. degree in electrical engineering from Sharif University of Technology, Tehran, Iran in 2018. She joined the Advanced Electric Machines and Power Electronics Lab at Texas A&M University, College Station, TX in 2018 and is currently working on her PhD in electrical engineering. Her research interest is electric machine design and optimization of electrified transportation systems.

**Matthew C. Gardner** (S'15, M'19) earned his B.S. in electrical engineering from Baylor University, Waco, Texas in 2014. He earned his Ph.D. in electrical engineering from Texas A&M University, College Station, Texas in 2019. In August 2020, he joined the University of Texas at Dallas, where he is an assistant professor. His research interests include optimal design and control of electric machines and magnetic gears.

**S. Mehdi Seyedi** (S'21) received his B.S. degree in Electrical Engineering with a minor in Power Engineering from Iran University of Science and Technology, Tehran, Iran, in 2013. He received his M.S. degree in Electrical Engineering in the field of Power Electronics and Electrical Machine Design from Iran University of Science and Technology, Tehran, Iran, in 2015. He joined the Advanced Electric Machines and Power Electronics lab at Texas A&M University in Spring 2021 as a Ph.D. student. His research interests include electrical machine design and control drives.

**Hamid A. Toliyat** (S'13, M'17) (S'87, M'91, SM'96, F'08) received the B.S, degree from Sharif University of Technology, Tehran, Iran in 1982, the M.S. degree from West Virginia University, Morgantown, WV in 1986, and the Ph.D. degree from University of Wisconsin–Madison, Madison, WI in 1991, all in electrical engineering. In March 1994 he joined the Department of Electrical and Computer Engineering, Texas A&M University where he is currently the Raytheon endowed professor of electrical engineering. Dr. Toliyat has many papers and awards to his name, including the Nikola Tesla Field Award.